JOURNAL OF GEOPHYSICAL RESEARCH, VOL. 111, A08106, doi:10.1029/2005JA011303, 2006

A global 2.5-dimensional three fluid solar wind model with alpha particles

Bo Li,[1] Xing Li,[1] and Nicolas Labrosse[1]

Received 5 July 2005; revised 21 April 2006; accepted 26 April 2006; published 24 August 2006.

[1] A global 2.5-dimensional three fluid solar wind model is presented. Two ion species, namely protons and alpha particles, are heated by an empirical energy flux while electrons are heated by the classical heat flux and Coulomb coupling with ions. It is found that for a reasonable relative speed between alpha particles and protons at 1 AU to be achieved, the alphas need to be preferentially heated in the inner corona. No external heating is applied in the streamer base, the closed magnetic field region. A hot coronal boundary, the electron heat flux, and Coulomb coupling keep plasma species in equilibrium inside the streamer, and a nonisothermal streamer is found. The abundance of alpha particles varies within the streamer base. It is small in the streamer core compared with streamer legs, and alphas continuously drain out of the streamer core along magnetic field due to gravitational settling. The settling operates over a timescale of several days. Alpha particles in the slow wind have a smaller abundance than in the fast wind at 1 AU, in agreement with observations. This is mainly determined in the near-Sun region. For the coronal alpha abundances in the range 0.015–0.15, it is found that alpha particles play a negligible role in determining the magnetic field. In this sense, treating alphas as test particles is justified. However, alphas have an important impact on solar wind parameters. Coulomb collisions and heating drag alphas into the solar wind. The Coulomb friction with protons by itself is, however, unable to drive into the slow solar wind a flux of alphas flowing at roughly the same speed of protons as observed by in situ measurements at 1 AU.

Citation: Li, B., X. Li, and N. Labrosse (2006), A global 2.5-dimensional three fluid solar wind model with alpha particles, *J. Geophys. Res.*, *111*, A08106, doi:10.1029/2005JA011303.

1. Introduction

[2] In situ measurements made by Helios beyond 0.3 AU indicate that in the fast solar wind, the flow speed of bulk helium ions (alpha particles) v_α is higher than that of protons v_p. The differential streaming $v_{\alpha p} = v_\alpha - v_p$ can be up to 150 km/s at 0.3 AU before decreasing with heliocentric distance r to 40 km/s at 1 AU [*Marsch et al.*, 1982]. To the contrary, $v_{\alpha p}$ in the slow wind is very low and shows no radial dependence. Although the ion temperature ratio $T_{\alpha p} = T_\alpha/T_p$ decreases with distance for both the slow and fast wind, $T_{\alpha p}$ in the fast wind is systematically higher than that in the slow one and yields a value of 3 at 1 AU. *Reisenfeld et al.* [2001] noted that this value is inconsistent with Ulysses measurements of the fast wind at heliocentric latitudes above 30°N which, when extrapolated to 1 AU, yield a value of 5. Given that Helios measurements are made in the ecliptic, the discrepancy in the derived temperature ratios may reflect that helium energetics is different for the fast wind at low and high latitudes [*Reisenfeld et al.*, 2001]. As to the alpha abundance $n_{\alpha p} = n_\alpha/n_p$, Ulysses measurements indicate that $n_{\alpha p}$ is about 0.045 in the fast wind at latitudes higher than 30° and hardly varies with latitude, whereas $n_{\alpha p}$ is highly variable in the slow wind, ranging from 0.004 to 0.1 [*McComas et al.*, 2000].

[3] In the extended corona, helium abundance has been derived from spectroscopic measurements made by two ultraviolet (UV) instruments aboard the Solar and Heliospheric Observatory (SOHO): the Solar Ultraviolet Measurements of Emitted Radiation (SUMER) and the Ultraviolet Coronagraph Spectrometer (UVCS). Using the SUMER data, *Laming and Feldman* [2003] compared the He II emission line with various lines and found that the helium abundance in coronal holes, with respect to hydrogen, may be no larger than that for typical fast wind. Helium therefore could already flow at least as fast as protons at an altitude of 0.05 to 0.13 R_S above the solar limb in polar coronal holes. The same authors [*Laming and Feldman*, 2001] obtained a helium abundance of He/H = 0.05 ± 0.0052 at about 1.177 R_S in the streamer base. This value agrees with the upper limit of 0.048, derived by *Raymond et al.* [1997a] who used UVCS He II Ba γ/H I Lyα ratio at 1.5 R_S.

[4] Further information about alpha behavior can be inferred from heavier ions such as O^{5+} for which direct measurements are possible. SOHO/UVCS observations show that in polar coronal holes, O^{5+} ions are more than

[1]Institute of Mathematical and Physical Sciences, University of Wales Aberystwyth, Aberystwyth, UK.

0148-0227/06/2005JA011303$09.00

mass-proportionally hotter than protons [*Esser et al.*, 1999]. They seem to flow significantly faster than protons as well, the outflow speed of O^{5+}s could reach 400 km/s at 3 R_S where the proton speed is less than 270 km/s [*Kohl et al.*, 1998; *X. Li et al.*, 1998]. On the other hand, coronal streamers, as measured by UVCS, are found to be morphologically different in O VI λ1032 and H I Lyα lines. The intensity ratio of O VI λ1032 to H I Lyα is smaller in the streamer core than in the legs [*Kohl et al.*, 1997]. In addition, there exists a sharp shear in O^{5+} outflow speed near the streamer border [*Habbal et al.*, 1997]. Further measurements by *Strachan et al.* [2002] suggest that the transition from no measurable speeds of O^{5+}s (in the core) to positive outflows can actually be used to infer the magnetic topology of the streamer. In streamer legs as well as the stalk, O^{5+} ions are found to be heated preferentially over protons but not so in the streamer core [*Frazin et al.*, 2003]. If one expects that different species of solar wind ions are heated/accelerated by the same mechanism, a flux of nonthermal energy for instance, alpha particles should exhibit a similar behavior.

[5] To explain the observations of ion species other than protons in the solar wind, many multifluid models have been developed, among which modeling efforts before 1980 have been reviewed by *Cuperman* [1980]. Modern one-dimensional (1-D) models have advanced to a point where sophisticated mechanisms such as the ion-cyclotron resonance are introduced to heat and accelerate the fast wind [e.g., *Isenberg and Hollweg*, 1983; *Hu and Habbal*, 1999; *Li*, 2003] or the slow wind [e.g., *Chen and Li*, 2004]. Naturally, multidimensional magnetohydrodynamic (MHD) models are needed to account for the magnetic field configuration and thus the flow tube geometry self-consistently. Ofman and coworkers have developed a series of 2.5-D three-fluid solar wind models, the first of which [*Ofman*, 2000] investigated the behavior of O^{5+} ions in the slow solar wind and coronal streamers. A similar study on alpha particles was carried out in the work of *Ofman* [2004a]. In the work of *Ofman and Davila* [2001], the authors explicitly introduced broadband low-frequency Alfvén waves and studied how these waves accelerate and heat the fast solar wind in coronal holes. This study was extended by *Ofman* [2004b] to take into account the heat conduction of both electrons and protons. In addition, empirical heating is applied to ions (including O^{5+}s or alphas).

[6] In this paper we conduct a numerical study on the acceleration and heating of the solar wind plasma which is composed of electrons (e), protons (p), and alphas (α). The computational domain extends from the coronal base to 1 AU and covers the latitudinal extent from the polar axis to the equator. Hence the fast solar wind and a streamer are studied in a single unified model. In this sense the model complements those by Ofman and coauthors [*Ofman*, 2000, 2004a, 2004b; *Ofman and Davila*, 2001] who paid special attention to the solar wind in the near-Sun regions and treat the acceleration of the fast wind and streamers in separate models. Ofman and his coworkers adopted a resistive MHD theory. However, the resistivity is neglected in this study. The configuration is assumed to be symmetrical about both the polar axis and the equator, so the model is only applicable to solar minimum conditions. The model is 2.5-D in essence since the azimuthal components of species velocities and the magnetic field are retained. To make the model as simple as possible, we shall employ an empirical energy flux to heat the ion species and neglect any volumetric force which may be associated with the energy deposition.

[7] The model is detailed in section 2. Specifically, we show in section 2.1 how the standard transport equations can be simplified under the assumption of azimuthal symmetry. Then we explain the numerical method as well as boundary conditions in section 2.2. The ion heating is described in section 2.3. Numerical results are presented in section 3. In addition to the reference model which is given in sections 3.1 and 3.2, we shall discuss the influence of alpha particles on the magnetic field (section 3.3) as well as the effect of ion heating on the alpha behavior at 1 AU (section 3.4). Section 4 gives a brief summary and concluding remarks.

2. Model Description

2.1. Derivation of Governing Equations

[8] In this section we show how to reduce the standard transport equations [e.g., *Schunk*, 1977, equation (24)] to the desired ones that govern the solar wind consisting of electrons, protons, and alpha particles. Each species s ($s = e$, p, α) is characterized by its mass m_s, electric charge e_s, density n_s, velocity $\mathbf{v}_s$, temperature T_s, and pressure $p_s = n_s k_B T_s$, where k_B is the Boltzmann constant. The species charge e_s can also be measured in units of electron charge e, i.e., $e_s = Z_s e$ with $Z_e \equiv -1$ by definition. Neglecting the electron inertia ($m_e \equiv 0$) in the electron momentum equation leads to an expression for the electric field $\mathbf{E}$

$$\mathbf{E} = -\frac{1}{c}\mathbf{v}_e \times \mathbf{B} - \frac{\nabla p_e}{n_e e} + \frac{1}{n_e e}\frac{\delta \mathbf{M}_e}{\delta t}, \tag{1}$$

where $\mathbf{B}$ is the magnetic field and c is the speed of light. Here $\delta\mathbf{M}_e/\delta t$ is the momentum exchange rate of electrons with other species from Coulomb collisions. Since the system evolves at a characteristic frequency far below the electron plasma frequency, quasi-neutrality can be safely assumed,

$$n_e = n_p + Z_\alpha n_\alpha. \tag{2}$$

The electron velocity $\mathbf{v}_e$ is related to ion velocities via the electric current density $\mathbf{j}$, i.e.,

$$\mathbf{v}_e = \mathbf{V} - \frac{\mathbf{j}}{n_e e}, \quad \mathbf{V} = \frac{n_p \mathbf{v}_p + Z_\alpha n_\alpha \mathbf{v}_\alpha}{n_e}, \quad \mathbf{j} = \frac{c}{4\pi}\nabla \times \mathbf{B}. \tag{3}$$

Using these relations, one can readily find the following governing equations,

$$\frac{\partial n_k}{\partial t} + \nabla \cdot (n_k \mathbf{v}_k) = 0, \tag{4}$$

$$\begin{aligned}\frac{\partial \mathbf{v}_k}{\partial t} &+ \mathbf{v}_k \cdot \nabla \mathbf{v}_k + \frac{\nabla p_k}{n_k m_k} + \frac{Z_k \nabla p_e}{n_e m_k} \\ &+ \frac{GM_S}{r^2}\hat{r} - \frac{Z_k}{4\pi n_e m_k}(\nabla \times \mathbf{B}) \times \mathbf{B} \\ &- \frac{1}{n_k m_k}\left[\frac{\delta \mathbf{M}_k}{\delta t} + \frac{Z_k n_k}{n_e}\frac{\delta \mathbf{M}_e}{\delta t}\right] \\ &+ \Omega_k \frac{n_j Z_j}{n_e}(\mathbf{v}_j - \mathbf{v}_k) \times \hat{\mathbf{b}} = 0,\end{aligned} \tag{5}$$

$$\frac{\partial \mathbf{B}}{\partial t} + c\nabla \times \left[-\frac{1}{c}\mathbf{V} \times \mathbf{B} + \frac{1}{4\pi n_e e}(\nabla \times \mathbf{B}) \times \mathbf{B} - \frac{\nabla p_e}{n_e e} \right] = 0, \tag{6}$$

$$\frac{\partial T_e}{\partial t} + \mathbf{v}_e \cdot \nabla T_e + (\gamma - 1) T_e \nabla \cdot \mathbf{v}_e + \frac{(\gamma - 1)}{n_e k_B} \nabla \cdot \mathbf{q}_e - \frac{(\gamma - 1)}{n_e k_B} \frac{\delta E_e}{\delta t} = 0, \tag{7}$$

$$\frac{\partial T_k}{\partial t} + \mathbf{v}_k \cdot \nabla T_k + (\gamma - 1) T_k \nabla \cdot \mathbf{v}_k - \frac{(\gamma - 1)}{n_k k_B} Q_k - \frac{(\gamma - 1)}{n_k k_B} \frac{\delta E_k}{\delta t} = 0, \tag{8}$$

where subscript k stands for ion species only ($k = p$, α). Subscript j in equation (5) refers to the ion species other than k, i.e., $j = \alpha$ for $k = p$ and vice versa. The ion-cyclotron frequency for species k is $\Omega_k = Z_k eB/m_k c$, $\hat{\mathbf{b}}$ is the unit vector along $\mathbf{B}$, G denotes the gravitational constant, and M_S is the solar mass. Here $\gamma = 5/3$ is the adiabatic index. The ion heating rate of species k, namely Q_k, will be given in section 2.3.

[9] In equation (6) the second term in the square parentheses is due to the Hall effect, whereas the third term represents the electric field from the electron pressure gradient. It is noted that the momentum exchange $\delta \mathbf{M}_e/\delta t$ is neglected when $\mathbf{E}$ is plugged into the magnetic induction law. The relative importance of the three terms in the square parentheses can be readily estimated. First of all, the ratio of the third to the second term is of order $8\pi p_e/B^2$, which is very small in the inner corona but comparable to unity in interplanetary space. The importance of the second term relative to the first one is

$$\frac{|\mathbf{j}|}{en_p|\mathbf{v}_p|} = \frac{c}{4\pi} \frac{|\nabla \times \mathbf{B}|}{en_p|\mathbf{v}_p|} \approx \frac{v_{A0}}{v_{p0}} \frac{c/\omega_{pp}}{L_0},$$

where $v_{A0} = \sqrt{B_0^2/4\pi n_{p0} m_p}$ is the proton Alfvén speed, $\omega_{pp} = \sqrt{4\pi n_{p0} e^2/m_p}$ is the proton plasma frequency. Subscript 0 denotes characteristic values for the designated parameters. L_0 is thus the spatial scale over which the magnetic field varies. This estimate usually leads to the conclusion that the Hall term is only important when the spatial scale in question is comparable with the proton inertial length c/ω_{pp} [e.g., *Huba*, 2003]. In the inner corona, c/ω_{pp} is on the order of kilometers, which is well below the spatial scale allowed by global fluid simulations. It is admittedly tricky to select appropriate values for other quantities in the above equation, especially when strong electric current concentrations are present (e.g., the streamer boundary). These two terms are therefore retained in the present study.

[10] We shall be concerned with configurations that are azimuthally symmetrical, i.e., $\partial/\partial\phi = 0$ is assumed in standard spherical coordinates (r, θ, ϕ). Let us explicitly distinguish the poloidal and azimuthal components of species velocities and the magnetic field,

$$\mathbf{B} = \mathbf{B}_P + B_\phi \hat{\phi}, \quad \mathbf{v}_k = \mathbf{v}_{kP} + v_{k\phi} \hat{\phi}, \tag{9}$$

where subscript P denotes the poloidal component. The assumption of azimuthal symmetry enables $\mathbf{B}_P$ to be expressed in terms of the magnetic flux function $\psi(r, \theta, t)$, namely,

$$\mathbf{B}_P = \nabla \times \left(\frac{\psi}{r \sin\theta} \hat{\phi} \right). \tag{10}$$

The Lorentz force in the momentum equation can therefore be written as

$$(\nabla \times \mathbf{B}) \times \mathbf{B} = -\mathcal{L}\psi \nabla \psi - \nabla \frac{B_\phi^2}{2} - B_\phi^2 \nabla \ln r \sin\theta + \left(\mathbf{B}_P \cdot \nabla B_\phi + B_\phi \mathbf{B}_P \cdot \nabla \ln r \sin\theta \right) \hat{\phi}, \tag{11}$$

where

$$\mathcal{L}\psi = \frac{1}{r^2 \sin\theta} \left(\frac{\partial^2 \psi}{\partial r^2} + \frac{1}{r^2} \frac{\partial^2 \psi}{\partial \theta^2} - \frac{\cot\theta}{r^2} \frac{\partial \psi}{\partial \theta} \right). \tag{12}$$

The magnetic induction equation (6) then becomes

$$\frac{\partial \psi}{\partial t} + \mathbf{V}_P \cdot \nabla \psi + \frac{c}{4\pi n_e e} \nabla \cdot \left(\mathbf{B}_P B_\phi r \sin\theta \right) = 0, \tag{13}$$

$$\frac{\partial B_\phi}{\partial t} + r \sin\theta \nabla \cdot \left[\frac{1}{r \sin\theta} \left(B_\phi \mathbf{V}_P - V_\phi \mathbf{B}_P \right) \right] + \hat{\phi} \cdot \left\{ \nabla \times \left[\frac{c}{4\pi n_e e} (\nabla \times \mathbf{B}) \times \mathbf{B} \right]_P \right\} + \hat{\phi} \cdot \left[\frac{c}{n_e^2 e} \nabla n_e \times \nabla p_e \right] = 0. \tag{14}$$

[11] The energy and momentum exchange rates $\delta E_s/\delta t$ and $\delta \mathbf{M}_s/\delta t$ are those from Coulomb collisions of species s with the remaining ones [*Schunk*, 1977],

$$\frac{\delta \mathbf{M}_s}{\delta t} = \sum_t n_s m_s \nu_{st} \Phi_{st} (\mathbf{v}_t - \mathbf{v}_s), \tag{15}$$

$$\frac{\delta E_s}{\delta t} = \sum_t \frac{n_s m_s \nu_{st}}{m_s + m_t} \left[3k_B (T_t - T_s) \Psi_{st} + m_t (\mathbf{v}_t - \mathbf{v}_s)^2 \Phi_{st} \right], \tag{16}$$

with [*Li et al.*, 1997]

$$\Phi_{st} = \frac{1}{1 + 0.74\epsilon_{st}^3}, \quad \Psi_{st} = \exp(-\epsilon_{st}^2), \tag{17}$$

$$\epsilon_{st} = \frac{|\mathbf{v}_t - \mathbf{v}_s|}{\sqrt{2k_B T_{st}/\mu_{st}}}, \tag{18}$$

$$T_{st} = \frac{m_s T_t + m_t T_s}{m_s + m_t}, \quad \mu_{st} = \frac{m_s m_t}{m_s + m_t}. \tag{19}$$

The collision frequency is

$$\nu_{st} = \frac{16\sqrt{\pi}}{3} \frac{n_t m_t}{m_s + m_t} \left(\frac{2k_B T_{st}}{\mu_{st}}\right)^{-3/2} \frac{e_s^2 e_t^2}{\mu_{st}^2} \ln\Lambda,$$

where the Coulomb logarithm ln Λ is taken to be 23 in this study. Such a value for ln Λ can be seen as an average between the coronal value and the one at 1 AU, since the solar wind expansion results in an electron density decreasing rapidly with r and therefore a modest increase in ln Λ. For the field-aligned electron conductive flux $\mathbf{q}_e$, the classical Spitzer-Harm law is adopted [*Spitzer*, 1962],

$$\mathbf{q}_e = -\kappa_e T_e^{5/2} \hat{\mathbf{b}}\hat{\mathbf{b}} \cdot \nabla T_e,$$

where $\kappa_e = 7.8 \times 10^{-7}$ erg·K$^{-7/2}$·cm^{-1}·s^{-1}. In the model, thermal conductivities of ions are neglected for simplicity.

2.2. Numerical Scheme and Boundary Conditions

[12] The ion-cyclotron term in equation (5), present in a two-ion fluid system, is a cross product of the ion velocity difference and the magnetic field. Hence the model can not be implemented in a strictly 2-D fashion. All the three components of species velocities and the magnetic field have to be retained instead, as has been explored in the context of solar wind massloading [e.g., *Sauer et al.*, 1994, 1996] and solar wind modeling [*Ofman*, 2004b]. This term is directly responsible for the ion-cyclotron waves (see, e.g., the linear analysis in section 3 of *Ofman et al.* [2005]).

[13] The ion-cyclotron term decreases the efficiency of numerical calculations dramatically, since the ion gyrofrequency is far larger than any other characteristic frequencies contained in the model equations. In practice, we solve equations (4) to (8) by adopting an operator-splitting method: A multistep implicit scheme [*Hu et al.*, 2003] is employed to handle all terms but the ion-cyclotron terms, which are then integrated implicitly [cf. *Ofman*, 2004b]. From an arbitrary initial state, model equations are advanced until a steady state is achieved.

[14] The computational box spans from the polar axis θ = 0° to the equator θ = 90°. Symmetrical conditions are assumed at these two boundaries. Unless explicitly stated, the radial extent of the computational box ranges from the coronal base (1 R_S) to the orbit of the Earth $R_E = 215R_S$. Be it placed at the orbit of the Earth or not, the top boundary is in the supersonic region, all the unknowns are simply extrapolated linearly. At the coronal base, the poloidal components of ion velocities, v_{kr} and $v_{k\theta}$, are determined by the conservation of mass flux for species k along poloidal flow tubes and the condition $\mathbf{v}_{kP} \parallel \mathbf{B}_P$. All azimuthal components are fixed at zero at 1 R_S.

[15] The magnetic flux that is initially open is set to be $\psi_c = 1.13 \times 10^{22}$ Mx, corresponding to a mean radial magnetic field of 5 γ at 1 AU. At 1 R_S, the magnetic flux ψ can be expressed as

$$\psi = \begin{cases} \dfrac{\zeta_0}{p+1}\left(1 - \cos^{p+1}\theta\right)\psi_c, & 0° \le \theta \le \theta_1, \\ \left[1 + \zeta_0 \cos^p\theta_1 (\cos\theta_2 - \cos\theta)\right]\psi_c, & \theta_1 \le \theta \le \theta_2, \\ \left[1 + \dfrac{\zeta_0 \cos^p\theta_1}{2\cos\theta_2}\left(\cos^2\theta_2 - \cos^2\theta\right)\right]\psi_c, & \theta_2 \le \theta \le 90°, \end{cases} \tag{20}$$

where

$$\zeta_0 = \frac{p+1}{1 - \cos^{p+1}\theta_1 + (p+1)\cos^p\theta_1(\cos\theta_1 - \cos\theta_2)}.$$

In the computation, $\theta_1 = 30°$, $\theta_2 = 60°$, and $p = 8$ are chosen. The magnetic flux contained in the initially closed field region is therefore $0.41\psi_c$. When equation (20) is derived, it is assumed that the radial magnetic field B_r scales as $B_r \propto \cos^p\theta$ for $\theta \le \theta_1$ and as $B_r \propto \cos\theta$ for $\theta_2 \le \theta \le 90°$, but is constant in the remaining area. Here $p = 8$ is chosen to be compatible with the observations for coronal holes [*Svalgaard et al.*, 1978]. The two regions [0, θ_1] and [θ_1, θ_2] can be regarded as open magnetic field regions inside and outside a polar coronal hole, respectively. Such a flux distribution is smoother than the original one in *Hu et al.* [2003] in that not only ψ but B_r are continuous with θ as well.

[16] Other base conditions are expressed with the aid of the function

$$S(x; x_1, y_1; x_2, y_2; n) = \sin^n\left(\frac{x - x_1}{x_2 - x_1}\frac{\pi}{2}\right)(y_2 - y_1) + y_1, \tag{21}$$

which connects points (x_1, y_1) and (x_2, y_2) smoothly. A power index n is used to control how (x_2, y_2) is approached. The base proton density is taken to be

$$n_p = 10^8 \mathrm{cm}^{-3} \times \begin{cases} S(\cos\theta; 1, 1.5; \cos\theta_2, 3; 2), & 0° \le \theta \le \theta_2 \\ 3, & \theta_2 \le \theta \le 90°. \end{cases} \tag{22}$$

The base alpha density is specified in terms of base abundance $n_{\alpha p}$. In the reference model a uniform value of $n_{\alpha p} = 0.065$ is used, regardless of the initial magnetic field topology. The base temperatures T_s are assumed to be the same for all species,

$$T_s = 10^6 \mathrm{K} \times \begin{cases} 1, & 0° \le \theta \le \theta_2 \\ 2, & \theta_2 \le \theta \le 90°. \end{cases} \tag{23}$$

Boundary conditions (22) to (23) come mainly from observational considerations and have been discussed in detail by *Hu et al.* [2003, section 2.2]. What differs from the original implementation in the work of *Hu et al.* [2003] is that the distribution of n_p is smoother: both n_p and its derivative with respect to θ are continuous.

2.3. Heat Deposition to Ions

[17] Equations (4) to (8) can be combined to give an energy conservation law. For a steady state, it reads

$$\nabla\cdot\left[\left(\frac{1}{2}n_pm_pv_p^2\mathbf{v}_p+\frac{1}{2}n_\alpha m_\alpha v_\alpha^2\mathbf{v}_\alpha\right)-\frac{GM_S}{r}\left(n_pm_p\mathbf{v}_p+n_\alpha m_\alpha\mathbf{v}_\alpha\right)+\frac{\gamma}{\gamma-1}\left(p_e\mathbf{v}_e+p_p\mathbf{v}_p+p_\alpha\mathbf{v}_\alpha\right)+\mathbf{q}_e\right]-\left(Q_p+Q_\alpha\right)=0. \quad (24)$$

The terms in the square brackets correspond to the fluxes of the kinetic and gravitational potential energy of particles, the enthalpy flux, and the electron heat flux, respectively. This conservation law can serve as a guide to specify the necessary heating parameters in the open magnetic field region.

[18] The ions are assumed to be heated by an empirical energy flux F launched by the Sun along $\mathbf{B}$. This empirical flux is dissipated at a rate Q over a characteristic length L, which results in

$$Q=F_E\frac{B}{B_EL}\exp\left(-\frac{r-R_S}{L}\right), \quad (25)$$

where $r-R_S$ roughly measures the arc length of the magnetic field line from the footpoint, F_E is the energy flux scaled to R_E. Both F_E and L are assumed to be dependent on ψ, which labels the magnetic field line. Hence they can be conveniently described as a function of $f_\psi=\psi/\psi_c$, namely,

$$F_E=1.9\times S\left(f_\psi;0,1;1,0.55;10\right)\text{erg cm}^{-2}\text{ s}^{-1}, \quad (26)$$

and

$$L=1.8\ R_S\times S\left(f_\psi;0,1;1,0.6;10\right). \quad (27)$$

[19] Q is then apportioned between protons and alpha particles according to the following relation,

$$Q_\alpha=\frac{\Delta}{1+\Delta},Q_p=\frac{1}{1+\Delta},\Delta=\frac{\rho_\alpha}{\rho_p}\chi, \quad (28)$$

where $\rho_k=n_km_k$ is the mass density of species k. Here χ is an indicator of how the alpha particles are preferentially heated, with $\chi\equiv1$ standing for the neutral heating: heating per ion is proportional to its mass. In practice, χ is set to be

$$\chi=\frac{\chi_\psi+0.8}{2}-\frac{\chi_\psi-0.8}{2}\tanh\left(\frac{r-5R_S}{0.3R_S}\right), \quad (29)$$

where

$$\chi_\psi=S\left(f_\psi;0,1.5;1,2;40\right). \quad (30)$$

As can be seen, χ is chosen to vary smoothly from a ψ-dependent value χ_ψ in the inner corona to 0.8 with a rather steep transition occurring at 5 R_S.

[20] We shall discuss in some detail the choice for the heating parameters. The latitudinal dependence is largely controlled by the power index n in function S (equation (21)) which is chosen by a trial-and-error method so that a transition from a relatively uniform fast wind to a slow wind occurs at about 75° at 1 AU, compatible with Ulysses measurements. The specification of the energy flux F_E is straightforward. For a typical fast (slow) wind at 1 AU, the proton flux n_pv_p (in 10^8 cm^{-2} s^{-1}) is 2 (3), the proton speed v_p is 800 (300) km/s and the alpha abundance $n_{\alpha p}$ is 0.04 (0.02). Assuming $v_\alpha=v_p$, one finds a typical energy flux (in erg cm^{-2} s^{-1}) is 2(1.26) for the fast (slow) solar wind. Since other energy sources may contribute to a lesser degree, the values for F_E are chosen slightly smaller than these two values. The dissipation length L is chosen such that the empirical heating is able to yield a proper proton flux. Both the heating function (equation (25)) and the manner, in which the dissipated energy is distributed between ion species (equation (28)), resemble the heating mechanism involving ion-cyclotron waves [cf. *Isenberg and Hollweg*, 1983; *Hu and Habbal*, 1999]. Previous calculations [e.g., *Hu and Habbal*, 1999] demonstrate that neutral heating ($\chi\equiv1$) results in alpha particles flowing slower than protons. A preferential heating ($\chi>1$) in the inner corona is necessary to drive into the solar wind a reasonable flux of alpha particles flowing at realistic speeds at 1 AU. Since we wish to achieve a differential speed $v_{\alpha p}$ decreasing with an increasing heliocentric radius r beyond some level in the fast wind, a radial dependence is introduced in equation (29).

3. Numerical Results

[21] It is necessary to give some general remarks on the solution. The system should evolve toward a steady state given that the heating parameters are time-independent. Moreover, since the solar rotation is not included, the azimuthal components prove negligible unless they appear alongside the ion-cyclotron frequency: They are only important in coupling the radial and latitudinal components of the ion momentum equations. We therefore neglect them completely in the following discussion, only poloidal components are described instead. In the open magnetic field regions, the convective electric field is the dominant part in equation (1). It follows from equation (13) that, in a steady state, the poloidal components of the electron velocity $\mathbf{v}_{eP}$ and magnetic field $\mathbf{B}_P$ must be parallel to a very good approximation. In addition, the ion-cyclotron frequency is by far the largest among the characteristic frequencies in the ion momentum equations (equation (5)). The ion velocity difference $\mathbf{v}_\alpha-\mathbf{v}_p$ must be aligned with the magnetic field $\mathbf{B}$. Combining these two facts, one can see that both $\mathbf{v}_{pP}$ and $\mathbf{v}_{\alpha P}$ should be in the direction of $\mathbf{B}_P$ when a steady state is reached. That is, when projected onto the meridional plane, all species should flow in the direction of the magnetic field.

3.1. Structure of the Streamer Base

[22] A good approximation to the density scale height of alpha particles is

$$H_\alpha=\frac{k_BT_\alpha}{m_\alpha g}\frac{1}{1-Z_\alpha/2A_\alpha}, \quad (31)$$

where alpha particles are seen as test particles only, g is the local gravitational acceleration. $A_\alpha=4$ is the mass number of alpha particles. The second term on the right-hand side of

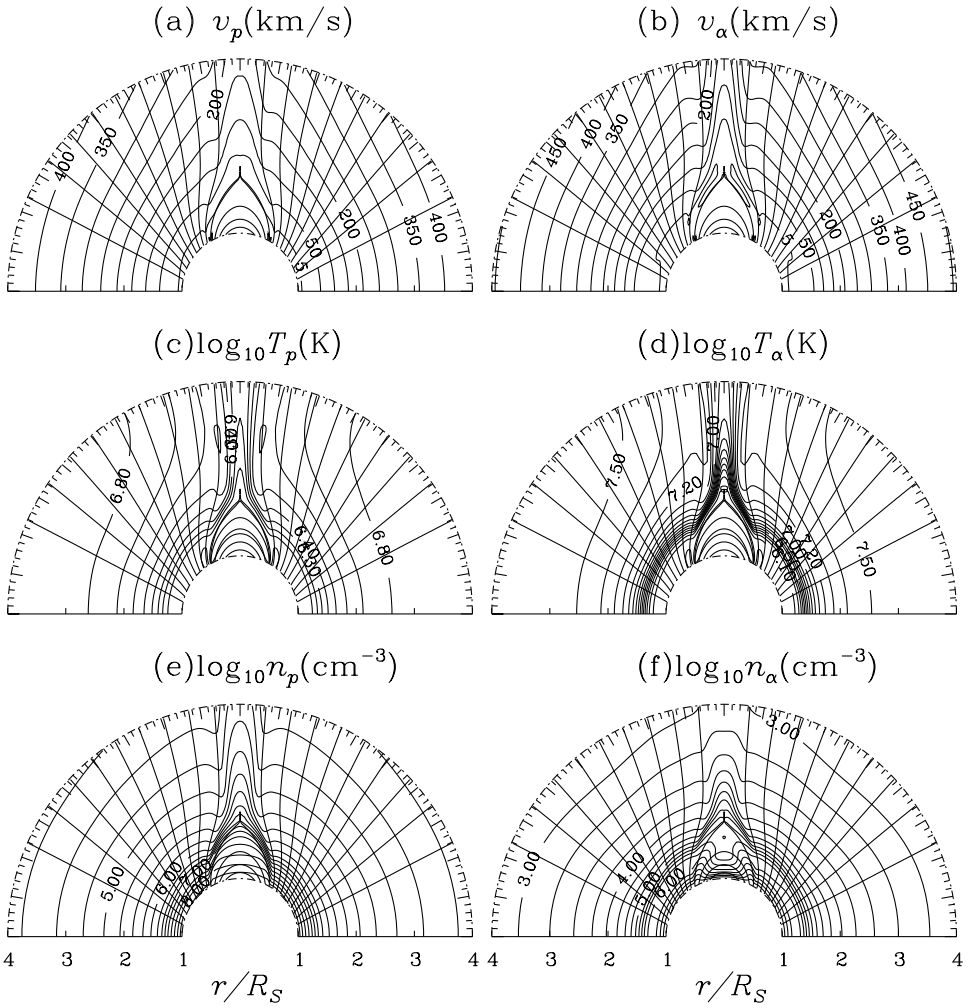

Figure 1. Global distributions of solar wind parameters at 150 hours derived from the 2.5-dimensional three fluid model which incorporates alpha particles. The magnetic field lines, given by background thin contours, are equally spaced by 0.1 ψ_c, ψ_c being the open flux. The polar axis corresponds to $\psi = 0$. Superimposed on the background are the contours of (a) and (b) outflow speed of protons v_p and α particles v_α, (c) and (d) temperature of protons T_p and α particles T_α, and (e) and (f) ion densities n_p and n_α. The flow speed contours are equally spaced by 50 km/s unless otherwise labeled, the logarithm of ion temperatures by 0.1, that of ion densities by 0.25.

equation (31) stems from the electric field due to the electron pressure gradient force which acts to enhance the ion scale height [see, e.g., *Lenz et al.*, 1998]. At a temperature of T_α = 2 MK, alpha particles will have a density scale height of 2×10^4km, or about 0.029 R_S at the coronal base. To resolve such a spatial scale, a fine grid is employed which is described as follows. In this section, the top boundary is placed at 15 R_S to save computational time. A computational box [1, 15] $R_S \times$ [0°, 90°] is discretized onto a 350 × 80 nonuniformly distributed grid. The radial grid spacing Δr increases from 0.005 R_S at 1 R_S to 0.117 R_S at 12.65 R_S and remains so until 15 R_S. As for the latitudinal grid spacing, $\Delta\theta$ decreases by a constant ratio from 3.64° at the pole to 0.7° at 59.2°, remaining constant thereafter.

[23] The steady state solar wind solution, in principle, does not depend on the initial state [*Hu et al.*, 2003]. This also turns out to be the case for the solar wind in the present computation, although different initial states may influence the speed with which the density structure inside the streamer core converges to a steady state. We therefore briefly describe the initial state. All the azimuthal components, $v_{p\phi}$, $v_{\alpha\phi}$ and B_ϕ are set to be zero. Both $v_{p\theta}$ and $v_{\alpha\theta}$ are taken to be zero as well. The temperatures decrease with radial distance r as $r^{-2/7}$, whereas the densities as r^{-3}. The radial velocities v_{pr} and $v_{\alpha r}$ are set equal and both vary smoothly with r from 1.1 km/s at the base to 500 km/s at the top. A partially open configuration with a cusp point located at 1.6 R_S is assumed for the magnetic field. After a physical time of 100 hours the system is nearly steady except for the density structure inside the streamer core.

[24] Figure 1 displays the system at t = 150 hours. To see the streamer in more detail, only the region below 4 R_S is shown. Here the equator points upward. The left side shows the contours of the proton speed ($v_p = \sqrt{v_{pr}^2 + v_{p\theta}^2}$), temperature ($T_p$), and density ($n_p$), whereas the right side gives

the alpha ones ($v_\alpha = \sqrt{v_{\alpha r}^2 + v_{\alpha\theta}^2}$, T_α, and n_α). The magnetic field configuration is shown using thin contours of the magnetic flux ψ equally spaced by $0.1\psi_c$. The polar axis corresponds to $\psi = 0$ and therefore $f_\psi = \psi/\psi_c = 0$. The cusp point is located at about 1.9 R_S, above which an equatorial current sheet separates opposite magnetic polarities. The most obvious latitudinal variations occur in the regions bordering the streamer base or around the current sheet. At higher latitudes, the latitudinal dependence of both proton and alpha parameters is relatively weak. In the streamer base the flow speeds of protons and alpha particles are below 5 km/s (Figures 1a and 1b). Moreover, there exists a sharp velocity shear for alpha particles (Figure 1b). If the same heating mechanism also acts on O^{5+}s, a similar velocity shear should be present, therefore providing an explanation for observations reported by *Habbal et al.* [1997].

[25] There are several interesting aspects concerning the ion temperatures T_p and T_α (Figures 1c and 1d). Both T_p and T_α experience a sharp change in the radial direction in the high-latitude region due to ion heating, but the change of T_α is even steeper, as evidenced by the contours concentrated around 1.4 R_S. Near the streamer boundary, T_α is much larger than T_p at $r > 1.5$ R_S. Careful examinations of Figures 1c and 1d show that protons and alpha particles have the same temperature everywhere in the closed magnetic field region: Coulomb coupling makes all the three species (e, p, and α) in local equilibrium in the absence of relative motions (see the first term on the right-hand side of equation (16)). A similar behavior has been observed for O^{5+} ions by *Frazin et al.* [2003], who show that the O^{5+} ions are hotter than protons in streamer legs below the visible cusp point but have the same temperature as protons within uncertainties in the streamer core.

[26] Despite a uniform base temperature (2 MK), the species temperature is nonuniform in the closed magnetic field region. An isothermal behavior is only reproduced in the region bounded by the magnetic field line which extends to 1.5 R_S at the equator. This is contrary to the conventional view that in streamers plasmas are isothermal (see section 4 for a discussion). To understand this, let us look at the electron energy equation (7) in a steady state and without motions,

$$\nabla \cdot \left(\kappa_e T_e^{5/2} \hat{\mathbf{b}}\hat{\mathbf{b}} \cdot \nabla T_e \right) = 0 \tag{32}$$

when all species are in equilibrium. It follows that

$$\frac{\kappa_e T_e^{5/2}}{B} \frac{\partial T_e}{\partial s} = \text{constant} \tag{33}$$

is true along a field line in the closed field region, where s is the distance along this field line. In general the relation above requires that the streamer is isothermal. $\partial T_e/\partial s \neq 0$ along the magnetic field is only valid if equation (33) is satisfied and $\partial T_e/\partial s$ is allowed to change sign at the equator. (The electron temperature itself is continuous of course.) This is only true at the cusp point. In the current numerical model, it turns out that a steady state is never really achieved in the region immediately below the cusp point. The high thermal pressure in the closed field region tends to open the magnetic field at the cusp point and the physics there is always time-dependent. This is likely the main reason that leads to the nonuniform temperature in the closed field region. To some degree, numerical diffusion may also contribute to this phenomena. A future study with an improved code efficiency and better computing resources will be needed to address the issue.

[27] The proton density n_p exhibits a nearly monotonical increase from the pole to the streamer base, a steep gradient appears at the streamer border. The proton density gradient stems from the transverse force balance, namely, the strong ambient magnetic pressure in the open field region is balanced by the enhanced thermal pressure of gases inside the streamer where $n_e = n_p$ is nearly true (cf. equation (35)). Now let us consider the parallel force balance inside the streamer base. Projecting equation (5) on the magnetic field line for both protons and alphas, one finds

$$\mathbf{B} \cdot \left[\nabla \left(p_e + p_\alpha + p_p \right) + \frac{\left(\rho_p + \rho_\alpha \right) GM_S}{r^2} \hat{r} \right] = 0. \tag{34}$$

In this region, alpha particles are of only minor importance. In addition, all the magnetic field lines of interest have identical base proton densities and temperatures. The proton gas therefore only sees the existence of a gravitational field that depends on r only. As a consequence, the proton density displays a nearly latitude-independent distribution. It also follows that the magnetic field is nearly potential inside this region, otherwise the θ component of the Lorentz force cannot be balanced. Beyond 1.5 R_S, the Lorentz force begins to play a role, the magnetic field is no longer potential [cf. *Hu et al.*, 2003].

[28] Similar to n_p, n_α undergoes a positive equatorward gradient from the fast wind region to the streamer border. However, n_α behaves in a manner opposite to n_p across the streamer boundary: n_α decreases when the core is approached. This is due to the fact that in the slow wind region, the preferential heating and Coulomb friction act to accelerate the alphas, dragging a significant amount of alphas into the wind. As a result, the density scale height is significantly enhanced. However, the alphas in the closed field regions suffer from gravitational settling which acts to drain alphas out of the corona, as will be discussed below.

[29] Figure 2 displays the latitudinal distribution across $r = 1.5$ R_S at $t = 150$ hours of ion densities n_p and n_α (Figure 2a) and radial speeds of protons v_{pr} and alphas $v_{\alpha r}$ (Figure 2b). In Figure 2a, the alpha densities at $t = 100$, 125, and 175 hours are also plotted by dotted, dashed, and dash-dotted lines, respectively. Besides, the vertical dash-dotted line delineates the streamer boundary which corresponds to $\psi/\psi_c = 1$, the streamer base lies to the right of this vertical bar. (Its location hardly varies after 100 hours.) It is obvious that the proton and alpha densities (Figure 2a) have distributions that are morphologically different, as far as the streamer is concerned. The streamer core is abundant with protons but short of alphas. However, although the alpha gas is tenuous, n_α is not strikingly low. For instance, n_α (in cm^{-3}) at the equator is 2.1×10^5, as opposed to hydrostatic value of less than 10^3. This overpopulation of alphas,

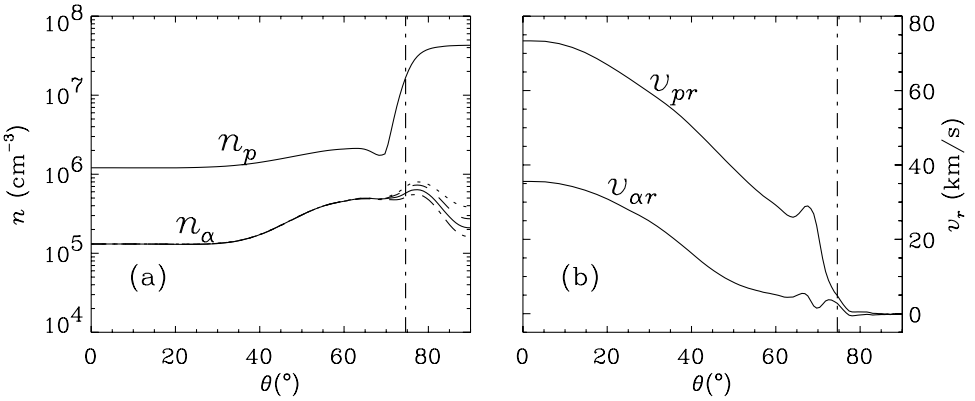

Figure 2. A latitudinal cut across $r = 1.5R_S$ at $t = 150$ hours. Distributions are shown by solid lines of (a) ion densities n_p and n_α, and (b) radial speeds of protons v_{pr} and alphas $v_{\alpha r}$. Figure 2a also shows the alpha densities at $t = 100$, 125, and 175 hours by dotted, dashed, and dash-dotted lines, respectively. Moreover, the vertical dash-dotted line stands for the streamer boundary, the streamer base lies to the right of this vertical bar.

compared with hydrostatic expectations, can be explained by the two-stage evolution of alpha population in the streamer base. During the first 100 hours, there is considerable mass exchange between different flux tubes. A considerable amount of alphas end up in the streamer base with n_α being orders of magnitude larger than its hydrostatic counterpart. However, after 100 hours, alphas only passively flow along the magnetic field **B** (Figure 2b). (For alpha particles, the only force balance that needs to be considered is that parallel to the magnetic field.) Whenever alphas develop a downward velocity, the protons will exert on them a frictional dragging force against the gravity. The relative speed between alphas and protons, although small, makes the Coulomb friction important owing to the high proton density. The parallel force balance of alphas is achieved by the projected gravity corrected for the electron effect, the alpha pressure gradient force and this Coulomb friction. This drain of alphas from the higher part of the arcade therefore only operates on a timescale of several days. For instance, within the interval from 100 to 175 hours, the alpha density n_α at the equator only decreases by 58% from 3.9 to 1.6×10^5 cm^{-3}. This kind of gravitational settling has already been discussed in detail by *Raymond et al.* [1997b] where O^{5+}s are considered.

[30] The parameters of alphas in Figure 2 may serve as a guide for designing future space-borne instruments to measure helium parameters in streamers, for which we do not have any empirical knowledge at the moment. In the two streamer legs, the density of alphas in the closed and open field regions are equally important. This implies that if observations find bright streamer legs in helium lines, we cannot safely say that the magnetic field in the bright regions are open.

3.2. Examination of Typical Fast and Slow Winds

[31] From now on, all computations will be made on a 200×60 grid which covers the computational box $[1, 215]$ $R_S \times [0°, 90°]$. The radial spacing Δr starts with 0.015 R_S at 1 R_S, increases to 0.27 R_S at 8.27 R_S, remains constant until 15 R_S, after which Δr increases steadily to 4.3 R_S at 107.5 R_S and does not vary thereafter. The smallest spacing Δr is comparable to the alpha density scale height at the base; this grid is therefore not sufficient to resolve the fine structure of alpha density inside the streamer base. Since the rarefied alpha gas (relative to protons) inside the streamer base has little impact on the magnetic field, this compromise is acceptable if one is only interested in the solar wind, channeled by open magnetic field lines by assumption. As to the latitudinal spacing $\Delta\theta$, it decreases from 4° at 0° to 1° at 60° and remains so until 90°.

[32] Figure 3 displays the distribution of several important parameters along two flow tubes that are representative of the fast (rooted at $\theta_b = 2°$ on the Sun, left column) and slow wind (rooted at $\theta_b = 57.5°$, right column). Figures 3a and 3b give the ion speeds and densities, while Figures 3c and 3d show species temperatures. In Figure 3a, the electron density (dashed lines) is also shown, hardly distinguishable from the proton one though. The temperature ratio $T_{\alpha p} = T_\alpha / T_p$ is plotted in Figures 3e and 3f, together with the flux tube expansion factor, defined as $f = Br^2/B_b$, B_b being the magnetic field strength at the footpoint of the tube.

[33] In the fast wind, Figure 3a indicates that the protons flow faster than the alpha particles below 2 R_S, beyond which the differential streaming, $v_{\alpha p} = v_\alpha - v_p$, increases steadily to 91 km/s at 6.84 R_S and decreases thereafter to an asymptotic value of 64.5 km/s at 1 AU. Moreover, the alpha speed displays a dip around 1.32 R_S where v_α possesses a local minimum of 7.4 km/s. This local stagnation originates from the steep increase in T_α profile (Figure 3c), the alpha pressure gradient force acts to decelerate alpha particles rather than accelerate them. The dip in v_α also results in a reduced expansion and consequently a flattened n_α profile. From the coronal base to 1.3 R_S, the Coulomb collisions between alpha particles and protons are still frequent enough to suppress a significant departure in T_p from T_α. However, beyond 1.3 R_S, T_α and T_p are no longer coupled, the preferential empirical heating results in $T_{\alpha p}$ becoming larger than $A_\alpha = 4$ beyond 1.66 R_S (Figure 3e). Owing to the assumed form of χ (equation (29)), the temperature ratio $T_{\alpha p}$ decreases after 5 R_S. Beyond about 10 R_S, $T_{\alpha p}$ is nearly constant. This comes from the fact that neither Coulomb collisions nor the heating is important in that region. Both protons and alphas cool adiabatically, resulting in T_p, $T_\alpha \propto r^{-4/3}$. As a consequence, the ratio $T_{\alpha p}$ does not depend on r

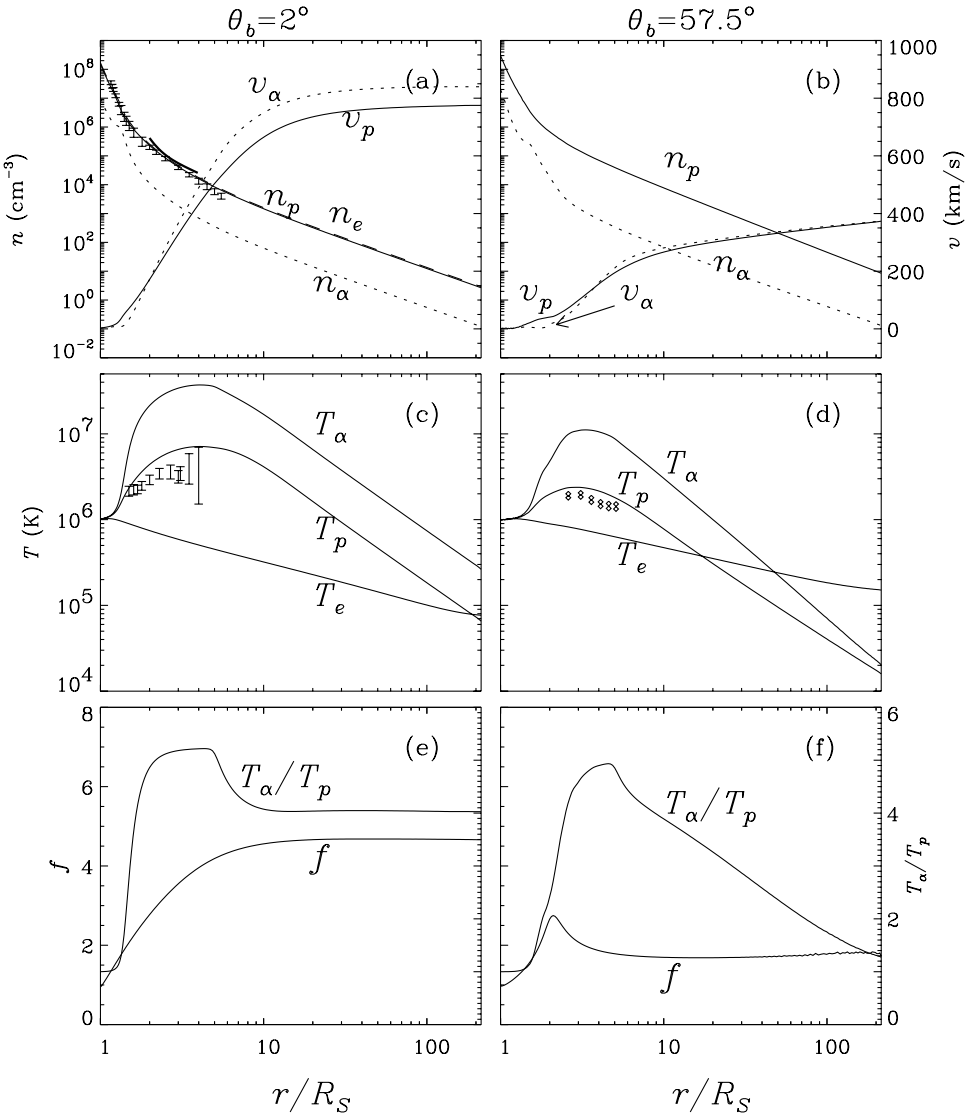

Figure 3. Radial profile of solar wind parameters along two flow tubes anchored at 2° (left column) and 57.5° (right column), representative of the fast and slow winds derived from the 2.5-D three fluid model. (a) and (b) Outflow speed and density of ion species. Moreover, in Figure 3a, the electron density n_e is also plotted (dotted line), the error bars represent the limits of electron density measured by *Fisher and Guhathakurta* [1995], the thick solid line between 2 and 4 R_S describes the empirical formula given by *Kohl et al.* [1998]. (c) and (d) Species temperatures. In Figure 3c, hydrogen I Lyα line width measurements are plotted by error bars [*Kohl et al.*, 1998], the open boxes in Figure 3d stand for the limits from similar measurements made for streamers by *Frazin et al.* [2003]. (e) and (f) The flow tube expansion factor f and the ion temperature ratio $T_{\alpha p} = T_\alpha/T_p$. f is defined as $f = B_b/Br^2$, B_b being the magnetic field strength at the footpoint.

any more. It can also be seen that without electron heating, the electron temperature T_e decreases monotonically with r (Figure 3c). The flux tube (Figure 3e) expands superradially below 10 R_S and f reaches an asymptotic value of 4.67 eventually.

[34] Let us compare the model results with some measurements available for the fast wind. At 1 AU the model yields a proton flux of $2.07 \times 10^8 \mathrm{cm}^{-2}\mathrm{s}^{-1}$, a proton speed of 775 km/s, and an alpha abundance $n_{\alpha p} = 0.045$, all of which agree well with Ulysses observations [*McComas et al.*, 2000]. The model incidentally yields a value of $T_{\alpha p} = 4$ at 1 AU, within the observed range of 3–5 [*Marsch et al.*, 1982; *Reisenfeld et al.*,2001]. However, both T_p and T_α are less than 1/4 of the observed [e.g., *McComas et al.*, 2000]. The cool ions as predicted by the present model are due to the adopted heating mechanism. The asymptotic differential streaming $v_{\alpha p}$ is 64.5 km/s, a value comparable to the local Alfvén speed, $v_A = B/\sqrt{4\pi\left(\rho_p + \rho_\alpha\right)}$ that yields 65 km/s in the model. In reality, $v_{\alpha p}$ however tends to be smaller than v_A [e.g., *Reisenfeld et al.*, 2001].

[35] Now let us turn to the comparison with the remote-sensing measurements of coronal holes, plotted in Figures 3a

and 3c. The error bars in Figure 3a give the upper and lower limit of electron densities measured by *Fisher and Guhathakurta* [1995], while the thick solid line between 2 and 4 R_S is from the empirical formula given by *Kohl et al.* [1998]. The modeled n_e profile can be seen to agree reasonably well with observations. However, as shown in Figure 3c, in the inner corona the modeled T_p is considerably higher than those inferred from H I Lyα line width measurements [*Kohl et al.*, 1998]. Assuming ion cyclotron waves are responsible for the coronal heating, *Li* [2003] showed that only alphas are directly heated by these waves. Coulomb coupling between protons and alphas is able to produce a proton temperature profile which matches these measurements.

[36] For the slow wind, a remarkable difference occurs in the profile of flow tube expansion factor f (Figure 3f). Unlike in the fast wind, f increases first to a maximum of 2.75 around the cusp and then falls off before increasing slowly to 1.73 asymptotically. The drastic lateral expansion of the flux tube is seen to be associated with the braked outflow of both protons and alpha particles (Figure 3b). This is especially true for the alpha flow, which shows a local minimum at about 1.8 R_S. This stagnated flow has been found by various authors from both 1-D [e.g., *Cuperman et al.*, 1990; *Wang*, 1994] and 2-D [e.g., *Yeh and Pneuman*, 1977; *Hu et al.*, 2003] studies where no additional ion species is taken into account. When O^{5+} ions are taken into account, the stagnated O^{5+} flow profile around the cusp has been found in the 2.5-D model by *Ofman* [2000] (see the bottom panel of his Figure 3) and recent 1-D models by *Chen and Li* [2004].

[37] In the slow wind, the differential speed $v_{\alpha p}$ is significantly smaller in magnitude than in the fast wind. Beyond 100 R_S, protons flow virtually at the same speed as alpha particles. Owing to the higher proton density, the ions are more strongly coupled. Although alphas are heated preferentially ($\chi = 2$ for $r < 5$ R_S), $T_{\alpha p} = T_\alpha/T_p$ (Figure 3f) is barely in excess of 1.2 at 1.6 R_S. The modeled $T_{\alpha p}$ barely exceeds the ion mass ratio $A_\alpha = 4$ between 2.52 and 8.8 R_S. Beyond 10 R_S, the Coulomb collisions still play a role in reducing the temperature ratio $T_{\alpha p}$.

[38] For the slow wind, the model predicts a proton flux 3.2×10^8 cm^{-2} s^{-1}, a proton speed 373 km/s, and an alpha abundance $n_{\alpha p} = 0.015$ at 1 AU. These values again agree well with Ulysses observations [*McComas et al.*, 2000]. In Figure 3d, the open boxes represent the upper and lower limits of proton effective temperatures, observed along a streamer stalk as reported by *Frazin et al.* [2003]. The modeled proton temperature is larger than the observed ones. At 1 AU, the resulting T_p and T_α are lower than in situ measurements. An interesting feature is that although no explicit electron heating is applied, the predicted T_e at 1 AU is consistent with in situ measurements in the slow wind [*Schwenn*, 1990].

[39] The alpha abundance at the coronal base is assumed to be the same for the slow and fast solar wind in this model. One, however, can see that the alpha abundance at 1 AU in the slow solar wind is significantly smaller than that in the fast wind. Actually, this is mainly determined in the near-Sun region. From the momentum equation (5), owing to the large mass of alpha particles, we can understand that even though Coulomb coupling is able to make species in equilibrium in the near-Sun region, proton-alpha friction is not strong enough to overcome the strong gravitational pull applied to alpha particles and to let alphas have the same flow speed as protons. If protons and alpha particles have the same temperature, alpha particles will always be decelerated relative to protons. The longer alpha particles and protons stay in equilibrium, the longer alpha particles remain to be decelerated relative to protons. This will lead to an even smaller ratio of v_α/v_p at the corona base and a smaller alpha flux.

[40] In the fast solar wind the preferential heating of alpha particles is more dramatic than in the slow wind in the near-Sun region. As a result, alpha particles decouple from protons at an earlier stage and have a higher temperature than protons. This is very important because in the alpha momentum equation, only the alpha pressure gradient force is able to give alpha particles a stronger acceleration relative to protons (due to their large mass). Since alpha particles and protons have roughly the same terminal speed in both the fast and slow solar wind, owing to mass conservation, using the above argument we find a smaller abundance of alpha particles in the slow than in the fast wind.

3.3. Influence of Alpha Particles on the Magnetic Field Configuration

[41] The parameter study by *Li et al.* [1997] shows that alpha particles can be dynamically important for an electron-proton background even when the coronal alpha abundance is as low as 5×10^{-4}. However, no similar investigation has been carried out into whether alphas are important in determining the magnetic parameters as well. We shall carry out such a study, using different base values for the alpha abundance (denoted by $n_{\alpha p,b}$) in the open magnetic field regions, while keeping all other parameters unchanged. Since the alpha gas inside the helmet is too tenuous to significantly contribute to the transverse force balance which determines the magnetic field, the alpha abundance at 1 R_S in the closed magnetic field regions is not varied.

[42] The proton and alpha momentum equations (5) can be combined to yield (note that Coulomb collisions are elastic),

$$\frac{\partial}{\partial \mathcal{N}}\left(p_T + \frac{B^2}{8\pi}\right) + \frac{GM_S}{r^2}\left(n_p m_p + n_\alpha m_\alpha\right)\sin\delta + \frac{1}{\mathcal{R}}\left(n_p m_p v_p^2 + n_\alpha m_\alpha v_\alpha^2 - \frac{B^2}{4\pi}\right) = 0, \tag{35}$$

where $p_T = p_e + p_p + p_\alpha$ is the total thermal pressure, $\mathcal{N}$ denotes the direction normal to the magnetic field, $\mathcal{R}$ denotes the curvature radius of the magnetic field line, and δ denotes the angle between the magnetic field and the radial direction. Those participating in the transverse force balance include the electron and ion thermal pressure, ion dynamic pressure, and the gravitational force. However, the dynamic pressures are associated with the magnetic field line curvature. When the flow is significant, as in high-latitude regions, the curvature is small, whereas when the curvature is significant, as in the region bordering the streamer base, the flow speed is only moderate. The gravitational force is also only of minor importance as the magnetic field does not

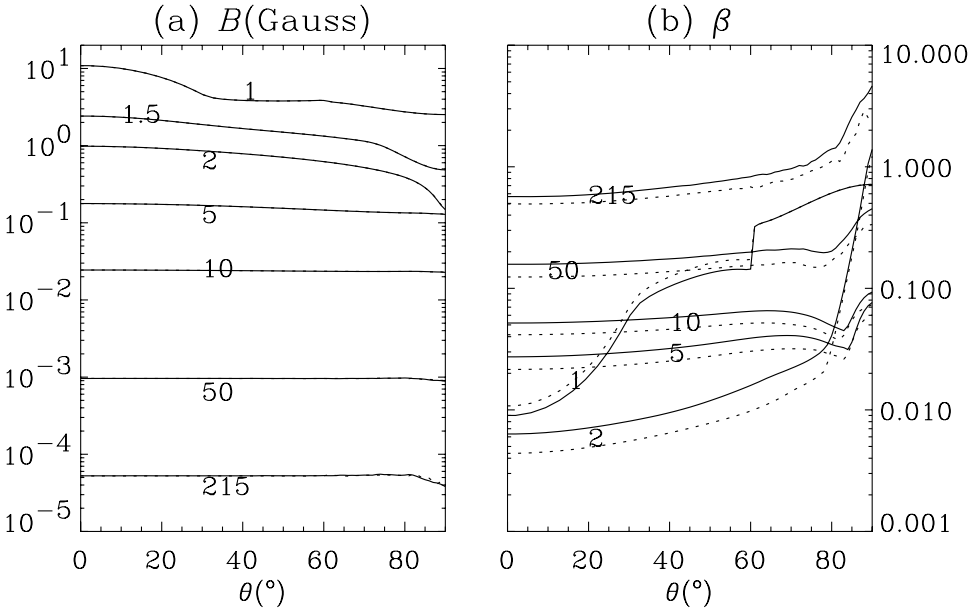

Figure 4. Comparison of models with different base alpha abundances $n_{\alpha p,b}$. Plotted are the latitudinal distributions of (a) the magnetic field strength B and (b) the plasma β at several radial distances as labeled. Solid lines are for $n_{\alpha p,b} = 0.015$, whereas dotted lines are for $n_{\alpha p,b} = 0.15$.

deviate significantly from the radial direction and the gravitational force itself is inversely proportional to r^2. Thus the transverse force balance is largely achieved by the thermal pressure and the magnetic field, whose relative importance can be measured by the plasma beta $\beta = 8\pi p_T/B^2$.

[43] Figure 4 compares two models with different base alpha abundances, namely $n_{\alpha p,b}$. Solid lines are used to plot the model with $n_{\alpha p,b} = 0.015$, whereas dotted lines are used for the model with $n_{\alpha p,b} = 0.15$. The latitudinal distributions of the magnetic field strength B (Figure 4a) and the plasma β (Figure 4b) are plotted at several radial distances as labeled. Although the base abundance changes by an order of magnitude, the difference in the B profile is not perceptible throughout the computational domain. This can be understood in light of the distributions of the plasma β, which on the one hand is only slightly changed but on the other hand is well below unity in most of the open field regions below 10 R_S. Also interesting is that with increasing radial distance, the latitudinal dependence of B is significantly reduced. This results in a nearly uniform B profile beyond 10 R_S, in agreement with Ulysses measurements [*Smith and Balogh*, 1995]. This relaxation in the latitudinal gradient of B stems from the β distribution. When $\beta \ll 1$ holds, as is the case below 10 R_S, the magnetic field must be nearly potential for the transverse force balance to be achieved. For a nearly radial magnetic field ($1/\mathcal{R} \approx 0$), this means B should be largely latitude-independent (see equation (35)).

[44] In addition, for $n_{\alpha p,b} = 0.15$, β is larger than that for $n_{\alpha p,b} = 0.015$ only at 1 R_S. At other distances, β for $n_{\alpha p,b} = 0.15$ is curiously smaller than that for $n_{\alpha p,b} = 0.015$. This behavior actually suggests that the alpha particles are dynamically important. As will be shown in Figure 5, increasing $n_{\alpha p,b}$ results in a smaller proton flux and a higher proton speed. Since the flux tube geometry is virtually unchanged ($n_p v_p/B$ is a tube constant), a larger proton flow combined with a smaller proton flux means a smaller proton density, which undermines the effect of an enhanced alpha pressure. The net effect is that the thermal pressure is reduced beyond some level between 1 and 2 R_S.

[45] Figure 5 displays the proton flux $n_p v_p$ (Figure 5a), the proton speed v_p (Figure 5b), the alpha abundance $n_{\alpha p}$ (Figure 5c), and the differential speed $v_{\alpha p}$ (Figure 5d) at 1 AU as a function of colatitude θ. Four models with different base alpha abundance $n_{\alpha p,b}$ are compared. Increasing $n_{\alpha p,b}$ systematically increases the alpha abundance $n_{\alpha p}$ at 1 AU (Figure 5c) as well as the differential speed $v_{\alpha p}$ (Figure 5d). In addition, it also results in a systematically reduced proton flux (Figure 5a) and an enhanced proton speed (Figure 5b). For instance, at $\theta = 0°$, the model with $n_{\alpha p,b} = 0.015$ (0.15) yields a proton flux (in 10^8 cm^{-2} s^{-1}) of 2.8 (1.48), and a proton speed of 693 (853) km/s. As far as the energy flux carried by the proton gas is concerned, the model with $n_{\alpha p,b} = 0.015$ (0.15) yields a value of 2.01 (1.37) erg·cm^{-2}·s^{-1}. The dependence on the base alpha abundance can be readily explained in view of the study by *Leer and Holzer* [1980]. With increasing $n_{\alpha p,b}$, more heating goes to alpha particles. The reduction of energy deposited in the subsonic region for proton gas results in a smaller proton flux, which means fewer protons are to share the dissipated mechanical energy flux, thereby giving rise to a higher energy per proton and thus a higher proton speed. Alpha particles are also heated more intensely closer to the Sun in the inner corona, resulting in a higher relative speed.

3.4. Role of Ion Heating on the Alpha Behavior in the Slow Wind

[46] Both the Coulomb friction and alpha pressure gradient force act to accelerate alpha particles, consequently alphas are more abundant in streamer legs compared to the core. The importance of Coulomb friction has been demonstrated by *Ofman* [2000]. It is therefore interesting to

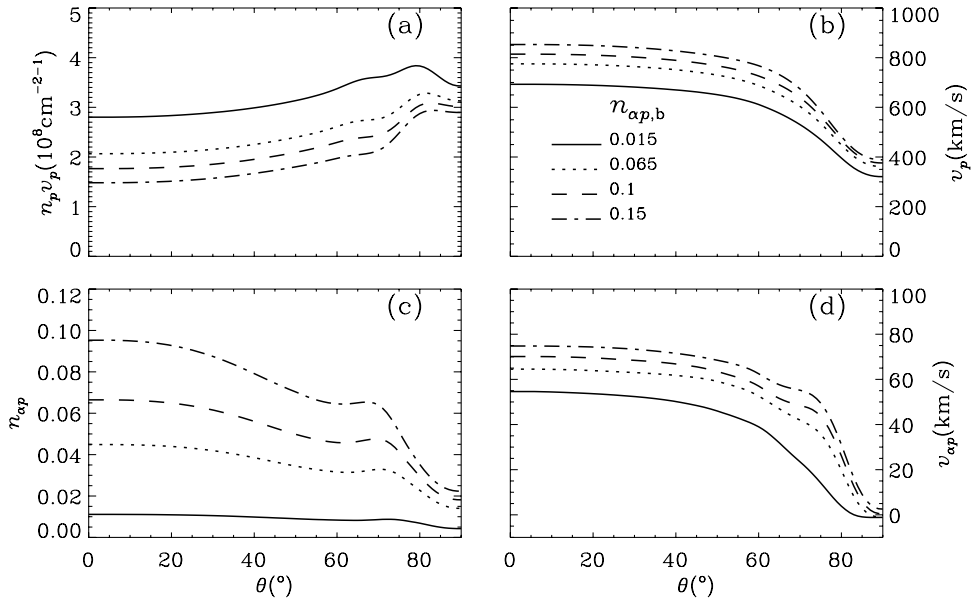

Figure 5. Comparison of models with different base alpha abundances $n_{\alpha p,b}$. Plotted are the distributions with colatitude θ at 1 AU of (a) proton flux $n_p v_p$, (b) proton speed v_p, (c) alpha abundance $n_{\alpha p}$ and (d) differential streaming $v_{\alpha p} = v_\alpha - v_p$. Different line styles are used for different $n_{\alpha p,b}$, as indicated in Figure 5b.

examine here the effect of ion heating. To this end, we compare two steady state models A and B. Model A is the reference model as has been presented, whereas model B is obtained by decreasing Q_α to 0.3 times the value in model A in regions for $0.8 \leq f_\odot \leq 1$. Figure 6 gives the distribution of the proton flux $n_p v_p$ (Figure 6a), the ion flux ratio $n_\alpha v_\alpha / n_p v_p$ (Figure 6b), the proton speed v_p (Figure 6c), and the alpha speed v_α (Figure 6d) at 1 AU as a function of colatitude θ. Solid and dashed lines are used to plot models A and B, respectively. Relevant Ulysses measurements [*McComas et al.*, 2000] are also plotted by dotted lines for comparison. It can be seen that Model A produces a fast wind that agrees quite well with Ulysses measurements, in terms of proton flux and proton speed, as well as ion flux ratio. Since only in the slow wind region is the alpha heating reduced, model B produces a fast wind solution

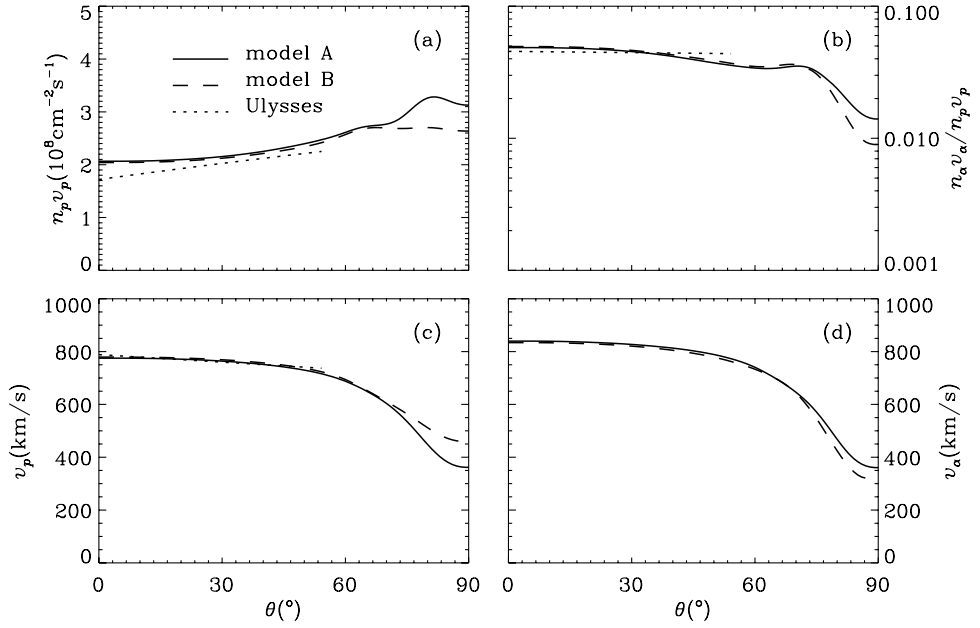

Figure 6. Latitudinal distributions at 1 AU of (a) proton flux $n_p v_p$, (b) ion flux ratio $n_\alpha v_\alpha / n_p v_p$, (c) proton speed v_p and (d) α speed v_α for two different models. In model B (dashed lines), the alpha heating rate is reduced to 0.3 times its original value in the reference model (model A, solid lines) in the slow wind region. Dotted lines give the empirical formula for the fast wind derived from Ulysses measurements [*McComas et al.*, 2000].

that virtually coincides with model A. This is understandable since the plasma contained in different flow tubes only communicate through the magnetic field, which is hardly affected by the changes of the flow properties in the slow wind region. The reduction in alpha heating not only reduces the ion flux ratio $n_\alpha v_\alpha / n_p v_p$ and the alpha terminal speed v_α but also leads to a reduction of proton flux $n_p v_p$ and an increase in terminal speed v_p. This is not surprising for the reasons discussed by *Leer and Holzer* [1980]. Now protons in model B can not gain as much energy as in model A from alpha particles, if not losing any instead. It follows that less energy is deposited to protons in the subsonic region; consequently a lower proton flux results. However the energy input per proton is larger, leading to a higher proton terminal speed. Note that although $n_\alpha v_\alpha / n_p v_p$ predicted by model B is 0.009 at the equator, still within the range measured by Ulysses over its first full polar orbit, the alphas lag behind the protons by 137 km/s at $\theta = 90°$, in contrast with the established fact that in the slow wind, alpha particles tend to flow at the same speed as protons. This suggests that external energy needs to be deposited to alpha particles in the corona to achieve a reasonable flux of alpha particles flowing at a realistic speed relative to protons. The Coulomb friction force exerted on alpha particles by protons alone is not sufficient to drive enough alpha particles into the solar wind and at the same time maintains a small terminal ion speed difference.

4. Summary and Discussion

[47] We have presented a 2.5-D global three fluid solar wind model consisting of electrons, protons, and alpha particles. The model extends from the coronal base to 1 AU, therefore enabling a comparison between modeled parameters and observations from both remote sensing and in situ measurements. As such, this model complements the models by Ofman and coauthors [*Ofman*, 2000; 2004a, 2004b; *Ofman and Davila*, 2001], where the solar wind in near-Sun regions is studied. Ion species are heated by an empirical energy flux, whereas the electrons by classical heat flux and Coulomb collisions with ions. No external heating apart from the electron heat flux and Coulomb coupling is applied to the closed field region. It is found that the simple empirical heating mechanism is able to produce proton speed and flux at 1 AU which are compatible with in situ measurements for both the slow and fast winds. By preferentially heating alpha particles in the inner corona, a reasonable differential speed $v_{\alpha p}$ can be achieved at 1 AU. It is found that the abundance of alpha particles varies within the streamer base. It is small in the streamer core compared to streamer legs, owing to gravitational settling which operates over a timescale of several days. For coronal alpha abundances in the range 0.015–0.15, alpha particles play a negligible role in the transverse force balance which determines the magnetic field configuration. In this sense it is justified to treat alpha particles as test particles. Alpha particles, however, have important effects on the solar wind parameters. Moreover, although playing an important part in the initial acceleration of alpha particles, the Coulomb friction with protons, by itself, cannot drag into the slow wind a flux of alpha particles flowing with a realistic speed relative to protons.

[48] One important difference of our model from *Ofman* [2004b] is the role of Coulomb collisions. In the near-Sun region, the proton density in the work of *Ofman* [2004b] is about 10 times higher than the proton density in the model presented in this work. For instance, at 5 solar radii in the polar fast solar wind, our proton density is roughly 10^4 cm^{-3} (Figure 3), and Figure 11 in the work of *Ofman* [2004b] gave a value above 10^5 cm^{-3}. Our proton density profiles in the fast solar wind give a better account for the solar wind observations at the solar minimum. An immediate effect of this difference is that Coulomb coupling plays a far less important role in our model in helping the alpha particles to escape the gravitational field.

[49] The heating mechanism chosen here is rather heuristic. The manner in which the dissipated mechanical energy is distributed among different ion species mimics the wave mechanism proposed by *Isenberg and Hollweg* [1983]. By doing so, we are able to specify how alpha particles are heated preferentially over protons. However, this simple approach is not able to account for some observational constraints. For instance, without taking into account the possible nonthermal motions, the predicted proton temperature T_p in the coronal hole is already larger than the effective temperature derived from H Lyα line-broadening measurements in the near-Sun region. Moreover, we adopt a r-dependent χ to produce a qualitatively correct profile of relative speed $v_{\alpha p}$: $v_{\alpha p}$ increases first and then decreases with r in the interplanetary space. Quantitatively, the magnitude of $v_{\alpha p}$ and its evolution deviate considerably from their observational counterparts.

[50] Before proceeding, we note that when fluid models are constructed, the specification of ion heating in the solar wind is by no means unique. As a matter of fact, *Sittler et al.* [2003] have followed a semiempirical approach in that they adopted a heat input in the form of effective heat flux estimated empirically by *Sittler and Guhathakurta* [1999]. Some improvements based on this spirit have been recently presented in section 3.3 of *Ofman* [2004a].

[51] In the collisionless region, the ion species only interact with each other through the electric field arising from the electron pressure gradient. This kind of collisionless coupling is not efficient since the electrons are cold in the computations. As a consequence, we are not able to reproduce the observed differential speed $v_{\alpha p}$ of 150 km/s at 0.3 AU decreasing to 40 km/s at 1 AU [*Marsch et al.*, 1982]. Many mechanisms have been proposed to decelerate the (relatively) streaming alpha particles in the interplanetary space [see *Kaghashvili et al.*, 2003, and references therein]. Among the candidates, various microinstabilities, the magnetosonic mode in particular, have received much attention because they have a threshold of $v_{\alpha p}$ that is in the order of the local Alfvén speed. In addition, it has been proposed that the rotational discontinuities and compressional waves generated by the nonlinear Alfvén waves can decelerate the streaming alphas, the kinetic energy being converted into perpendicular as well as parallel heating [*Kaghashvili et al.*, 2003]. If these mechanisms can be incorporated into fluid models, a better agreement between modeled ion temperatures and in situ measurements can also be expected.

[52] Without explicit external heating, it is found that a hot coronal base, Coulomb coupling, and electron heat flux can produce a nonisothermal streamer. This does not contradict the analysis of *J. Li et al.* [1998] who concluded that on the one hand, the temperature measured at 1.15 R_S and 1.5 R_S in the streamer is equal within uncertainty, on the other hand, the electron densities measured at these two altitudes agree with the profile derived from the hydrostatic equilibrium. These observations are indeed reproduced in our numerical solutions. A future study is needed to explore the transition from the streamer to the solar wind.

[53] In the models of this paper, the electron temperature never exceeds 1.1 MK in the solar wind at $r < 1.5\ R_S$. This behavior is in line with SOHO coronal hole electron temperature observations below 1.3 solar radii [*David et al.*, 1998; *Wilhelm et al.*, 1998]. However, it is at variance with the values derived from ion charge state measurements [e.g., *Geiss et al.*, 1995; *Ko et al.*, 1997]. Two mechanisms have been proposed to remove this discrepancy, without violating the SUMER line ratio measurements by *Wilhelm et al.* [1998]. *Esser and Edgar* [2000] suggested a population of hot electrons in the inner corona may remove the discrepancy. On the other hand, *Laming* [2004] argued that the O VI diagnostic used by *David et al.* [1998] should be sensitive to the hot electron component but no such evidence was found. The hot electron component should also interact strongly with the cold core component due to Coulomb collisions. *Laming* [2004] suggested that electrons at $R > 1.3$ solar radii are heated by lower hybrid waves generated by gyrating minor ions in the presence of a density gradient. He argued the collisionless nature of electrons makes the electron heat flux to be zero and no heat due to the electron heating will be conducted to the region below 1.3 solar radii (to contradict observations). Obviously, this is a complex issue beyond the scope of this paper. We agree that electrons need some heating in interplanetary space. It is noted, however, that *Laming* [2004] argued the importance of Coulomb collisions to reject the proposal of *Esser and Edgar* [2000] and then had to assume that electrons are collisionless to justify his assumption of zero electron heat flux. Some previous studies also suggested the classical electron heat flux formulation may be still valid at least in the near-Sun region [*Li*, 1999; *Olsen and Leer*, 1999].

[54] The treatment of the electron conductive flux $\mathbf{q}_e$ also needs some justification. In this paper the collision-dominated classical Spitzer law is assumed for $\mathbf{q}_e$. Such an expression may become questionable beyond a certain distance where electrons become collisionless. *Hollweg* [1974] proposed an approach to tackle this problem by dividing the computational domain into two parts: The inner one assumes the Spitzer law, whereas the outer one assumes an ansatz for $\mathbf{q}_e$ to account for the collisionless nature of electrons. The two approaches, however, seem to give little difference in terms of the proton terminal speed and flux [*Li et al.*, 2005].

[55] In 1-D three-fluid models, the ion-cyclotron resonance has been invoked to account for a number of observed features in the fast as well as slow solar wind [e.g., *Hu and Habbal*, 1999; *Li*, 2003; *Chen and Li*, 2004]. This work can be improved by replacing the empirical heating with the ion cyclotron resonance which may be able to produce a more realistic radial profile of ion differential streaming owing to the resonant acceleration of ions. Another application of the present model is to include O^{5+} ions, whose direct measurements in the inner corona are currently available [e.g., *Frazin et al.*, 2003; *Strachan et al.*, 2002]. So far, the only attempt to model the global distribution of the O VI emissivity is made by *Vásquez and Raymond* [2005] who assumed ionization balance for Oxygen to compute the O^{5+} population. In our treatment, the minor ion population is determined by dynamical processes. It is therefore interesting to rederive the emissivity distributions and compare them with available measurements.

[56] In the present model the magnetic field within the streamer core remains closed during relaxation. However, when external heating is applied to closed field regions, the magnetic flux could be stripped of the streamer and open to the interplanetary space. Energy sink such as the downward electron heat flux is unable to quench this process completely [*Suess et al.*, 1996]. Both protons and alpha particles contained in the streamer could escape into the solar wind. Consequently, the slow wind may have two origins, one from the initially open field regions bordering the streamer, the other from the gradually opened regions. Since the two regions have different properties concerning alpha distributions, the resulting alpha abundance at 1 AU could well be variable, as have been commonly observed at 1 AU in the slow solar wind. We will report this work in another publication.

[57] **Acknowledgments.** This work was supported by a PPARC rolling grant to the University of Wales Aberystwyth. The authors thank both referees for their thorough and constructive comments.

[58] Arthur Richmond thanks the reviewers for their assistance in evaluating this paper.

References

Chen, Y., and X. Li (2004), An ion-cyclotron resonance-driven three-fluid model of the slow wind near the Sun, *Astrophys. J.*, *609*, L41–L44.

Cuperman, S. (1980), Plasma field aspects of the solar wind, *Space Sci. Rev.*, *26*, 277–315.

Cuperman, S., L. Ofman, and M. Dryer (1990), Thermally conductive magnetohydrodynamic flows in helmet-streamer coronal structures, *Astrophys. J.*, *350*, 846–855.

David, C., et al. (1998), Measurement of the electron temperature gradient in a solar coronal hole, *Astron. Astrophys.*, *336*, L90–L94.

Esser, R., and R. J. Edgar (2000), Reconciling spectroscopic electron temperature measurements in the solar corona with in situ charge state observations, *Astrophys. J.*, *532*, L71–L74.

Esser, R., S. Fineschi, D. Dobrzycka, S. R. Habbal, R. J. Edgar, J. C. Raymond, J. Kohl, and M. Guhathakurta (1999), Plasma properties in coronal holes derived from measurements of minor ion spectral lines and polarized white light intensity, *Astrophys. J.*, *510*, L63–L67.

Fisher, R., and M. Guhathakurta (1995), Physical properties of polar coronal rays and holes as observed with the SPARTAN 201-01 coronagraph, *Astrophys. J.*, *447*, L139–L142.

Frazin, R. A., S. R. Cranmer, and J. L. Kohl (2003), Empirically determined anisotropic velocity distributions and outflows of O^{5+} ions in a coronal streamer at solar minimum, *Astrophys. J.*, *597*, 1145–1157.

Geiss, J., et al. (1995), The southern high-speed stream - results from the SWICS instrument on ULYSSES, *Science*, *268*, 1033–1036.

Habbal, S. R., R. Woo, S. Fineschi, R. O'Neal, J. Kohl, G. Noci, and C. Korendyke (1997), Origins of the slow and the ubiquitous fast solar wind, *Astrophys. J.*, *489*, L103–L106.

Hollweg, J. V. (1974), Electron heat-conduction in solar-wind, *J. Geophys. Res.*, *79*, 3845–3850.

Hu, Y. Q., and S. R. Habbal (1999), Resonant acceleration and heating of solar wind ions by dispersive ion cyclotron waves, *J. Geophys. Res.*, *104*, 17,045–17,056.

Hu, Y. Q., S. R. Habbal, Y. Chen, and X. Li (2003), Are coronal holes the only source of fast solar wind at solar minimum?, *J. Geophys. Res.*, *108*(A10), 1377, doi:10.1029/2002JA009776.

Huba, J. D. (2003), Hall magnetohydrodynamics: A tutorial, in *Space Plasma Simulation*, *Lecture Notes in Phys.*, vol. 615, edited by J. Bchner, C. Dum, and M. Scholer, pp. 166–192, Springer, New York.

Isenberg, P. A., and J. V. Hollweg (1983), On the preferential acceleration and heating of solar wind heavy ions, *J. Geophys. Res.*, *88*, 3923–3935.

Kaghashvili, E. K., B. J. Vasquez, and J. V. Hollweg (2003), Deceleration of streaming alpha particles interacting with waves and imbedded rotational discontinuities, *J. Geophys. Res.*, *108*(A1), 1036, doi:10.1029/2002JA009623.

Ko, Y.-K., L. A. Fisk, J. Geiss, G. Gloeckler, and M. Guhathakurta (1997), An empirical study of the electron temperature and heavy ion velocities in the south polar coronal hole, *Sol. Phys.*, *171*, 345–361.

Kohl, J. L., et al. (1997), First results from the SOHO Ultraviolet Coronagraph Spectrometer, *Sol. Phys.*, *175*, 613–644.

Kohl, J. L., et al. (1998), UVCS/SOHO empirical determinations of anisotropic velocity distributions in the solar corona, *Astrophys. J.*, *501*, L127–L131.

Laming, J. M. (2004), On collisionless electron-ion temperature equilibration in the fast solar wind, *Astrophys. J.*, *604*, 874–883.

Laming, J. M., and U. Feldman (2001), The solar Helium abundance in the outer corona determined from observations with SUMER/SOHO, *Astrophys. J.*, *546*, 552–558.

Laming, J. M., and U. Feldman (2003), The variability of the solar coronal Helium abundance: Polar coronal holes compared to the quiet sun, *Astrophys. J.*, *591*, 1257–1266.

Leer, E., and T. E. Holzer (1980), Energy addition in the solar wind, *J. Geophys. Res.*, *85*, 4681–4688.

Lenz, D. D., Y.-Q. Lou, and R. Rosner (1998), Density structure in a multicomponent coronal loop, *Astrophys. J.*, *504*, 1020–1028.

Li, J., J. C. Raymond, L. W. Acton, J. L. Kohl, M. Romoli, G. Noci, and G. Naletto (1998), Physical structure of a coronal streamer in the closed-field region as observed from UVCS/SOHO and SXT/Yohkoh, *Astrophys. J.*, *506*, 431–438.

Li, X. (1999), Proton temperature anisotropy in the fast solar wind: A 16-moment bi-Maxwellian model, *J. Geophys. Res.*, *104*, 19,773–19,785.

Li, X. (2003), Transition region, coronal heating and the fast solar wind, *Astron. Astrophys.*, *406*, 345–356.

Li, X., R. Esser, S. R. Habbal, and Y. Q. Hu (1997), Influence of heavy ions on the high-speed solar wind, *J. Geophys. Res.*, *102*, 17,419–17,432.

Li, X., S. R. Habbal, J. Kohl, and G. Noci (1998), The effect of temperature anisotropy on observations of Doppler dimming and pumping in the inner corona, *Astrophys. J.*, *501*, L133–L137.

Li, B., S. R. Habbal, X. Li, and C. Mountford (2005), Effect of the latitudinal distribution of temperature at the coronal base on the interplanetary magnetic field configuration and the solar wind flow, *J. Geophys. Res.*, *110*, A12112, doi:10.1029/2005JA011332.

Marsch, E., K.-H. Mühlhäuser, H. Rosenbauer, R. Schwenn, and F. M. Neubauer (1982), Solar wind helium ions: Observations of the Helios solar probes between 0.3 and 1 AU, *J. Geophys. Res.*, *87*, 35–51.

McComas, D. J., B. L. Barraclough, H. O. Funsten, et al. (2000), Solar wind observations over Ulysses' first full polar orbit, *J. Geophys. Res.*, *105*, 10,419–10,434.

Ofman, L. (2000), Source regions of the slow solar wind in coronal streamers, *Geophys. Res. Lett.*, *27*, 2885–2888.

Ofman, L. (2004a), The origin of the slow solar wind in coronal streamers, *Adv. Space Res.*, *33*, 681–688.

Ofman, L. (2004b), Three-fluid model of the heating and acceleration of the fast solar wind, *J. Geophys. Res.*, *109*, A07102, doi:10.1029/2003JA010221.

Ofman, L., and J. M. Davila (2001), Three-Fluid 2.5-dimensional Magnetohydrodynamic model of the effective temperature in coronal holes, *Astrophys. J.*, *553*, 935–940.

Ofman, L., A. Viñas, and S. P. Gary (2001), Constraints on the O^{+5} anisotropy in the solar corona, *Astrophys. J.*, *547*, L175–L178.

Ofman, L., J. M. Davila, V. M. Nakariakov, and A.-F. Vias (2005), High-frequency Alfvn waves in multi-ion coronal plasma: Observational implications, *J. Geophys. Res.*, *110*, A09102, doi:10.1029/2004JA010969.

Olsen, L., and E. Leer (1999), A study of solar wind acceleration based on gyrotropic transport equations, *J. Geophys. Res.*, *104*, 9963.

Raymond, J. C., et al. (1997a) Composition of coronal streamers from the SOHO Ultraviolet Coronagraph Spectrometer, *Sol. Phys.*, *175*, 645–665.

Raymond, J. C., R. M. Suleiman, A. A. van Ballegooijen, and J. L. Kohl (1997b), Absolute abundances in streamers from UVCS, in *Correlated Phenomena at the Sun, in the Heliosphere and in Geospace*, edited by A. Wilson, *Eur. Space Agency Spec. Publ., ESA SP-415*, 383–386.

Reisenfeld, D. B., S. P. Gary, J. T. Gosling, and J. T. Steinberg (2001), Helium energetics in the high-latitude solar wind: Ulysses observations, *J. Geophys. Res.*, *106*, 5693–5708.

Sauer, K., A. Bogdanov, and K. Baumgartel (1994), Evidence of an ion composition boundary (protonopause) in bi-ion fluid simulations of solar wind mass loading, *Geophys. Res. Lett.*, *21*, 2255–2258.

Sauer, K., E. Dubinin, K. Baumgärtel, and A. Bogdanov (1996), Bow shock 'splitting' in bi-ion flows, *Geophys. Res. Lett.*, *23*, 3643–3646.

Schunk, R. W. (1977), Mathematical structure of transport equations for multispecies flows, *Rev. Geophys.*, *15*, 429–445.

Schwenn, R. (1990), Large-scale structure of the interplanetary medium, in *Physics of the Inner Heliosphere I, Large Scale Phenomena*, edited by R. Schwenn and E. Marsch, p. 99, Springer, New York.

Sittler, E. C., and M. Guhathakurta (1999), Semiempirical two-dimensional MagnetoHydrodynamic model of the solar corona and interplanetary medium, *Astrophys. J.*, *523*, 812–826.

Sittler, E. C., L. Ofman, S. Gibson, M. Guhathakurta, J. Davila, R. Skoug, A. Fludra, and T. Holzer (2003), Development of multidimensional MHD model for the solar corona and solar wind, in *Solar Wind 10*, edited by M. Velli, R. Bruno, and F. Malara, *AIP Conf. Proc.*, *679*, 113–116.

Smith, E. J., and A. Balogh (1995), Ulysses observations of the radial magnetic field, *Geophys. Res. Lett.*, *22*, 3317–3320.

Spitzer, L., Jr. (1962), *Physics of Fully Ionized Gases*, Wiley Interscience, Hoboken, N.J.

Strachan, L., R. Suleiman, A. V. Panasyuk, D. A. Biesecker, and J. L. Kohl (2002), Empirical densities, kinetic temperatures, and outflow velocities in the equatorial streamer belt at solar minimum, *Astrophys. J.*, *571*, 1008–1014.

Suess, S. T., A.-H. Wang, and S. T. Wu (1996), Volumetric heating in coronal streamers, *J. Geophys. Res.*, *101*, 19,957–19,966.

Svalgaard, L., T. L. Duvall, and P. H. Scherrer (1978), The strength of the sun's polar fields, *Sol. Phys.*, *58*, 225–239.

Vásquez, A. M., and J. C. Raymond (2005), Oxygen abundance in coronal streamers, *Astrophys. J.*, *619*, 1132–1141.

Wang, Y. M. (1994), Two types of slow solar wind, *Astrophys. J.*, *437*, L67–L70.

Wilhelm, K., E. Marsch, B. N. Dwivedi, D. M. Hassler, P. Lemaire, A. H. Gabriel, and M. C. E. Huber (1998), The solar corona above polar coronal holes as seen by SUMER on SOHO, *Astrophys. J.*, *500*, 1023–1038.

Yeh, T., and G. W. Pneuman (1977), A sheet-current approach to coronal-interplanetary modeling, *Sol. Phys.*, *54*, 419–430.

N. Labrosse, B. Li, and X. Li, Institute of Mathematical and Physical Sciences, University of Wales Aberystwyth, Aberystwyth SY23 3BZ, UK. (nll@aber.ac.uk; bbl@aber.ac.uk; xxl@aber.ac.uk)